PVDF membranes containing hybrid nanoparticles for adsorbing cationic dyes: physical insights and mechanism

2016 Mater. Res. Express 3 075303

(http://iopscience.iop.org/2053-1591/3/7/075303)

Materials Research Express

PAPER

PVDF membranes containing hybrid nanoparticles for adsorbing cationic dyes: physical insights and mechanism

Maya Sharma[1], **Giridhar Madras**[2] **and Suryasarathi Bose**[3]

[1] Center for Nano Science and Engineering, Indian Institute of Science, Bangalore-560012, India
[2] Department of Chemical Engineering, Indian Institute of Science, Bangalore-560012, India
[3] Department of Materials Engineering, Indian Institute of Science, Bangalore-560012, India

E-mail: sbose@materials.iisc.ernet.in

RECEIVED
3 February 2016

REVISED
20 June 2016

ACCEPTED FOR PUBLICATION
24 June 2016

PUBLISHED
22 July 2016

Keywords: Fe_2O_3, solution combustion method, chlorinated cationic dyes, PVDF, phase inversion

Abstract

In this study, Fe (iron) and Ag (silver) based adsorbents were synthesized using solution combustion and *in situ* reduction techniques. The synthesized adsorbents were comprehensively characterized by different techniques including electron microscopy, BET, XRD, Zeta potential etc. Three chlorinated cationic dyes used were malachite green, methyl violet and pyronin Y. These dyes were adsorbed on various synthesized adsorbents [iron III oxide (Fe_2O_3)], iron III oxide decorated silver nanoparticles by combustion synthesis technique [Fe_2O_3–Ag(C)] and iron III oxide decorated silver nanoparticles using *in situ* reduction, [Fe_2O_3–Ag (S)]. The isotherm and the adsorption kinetics have been studied systematically. The kinetic data can be explained by the pseudo second order model and the adsorption equilibrium followed Langmuir isotherm. The equilibrium and kinetics results suggest that Fe_2O_3–Ag(S) nanoparticles showed the maximum adsorption among all the adsorbents. Hence, Polyvinylidene fluoride based membranes containing Fe_2O_3–Ag(S) nanoparticles were prepared via phase inversion (precipitation immersion using DMF/water) technique. The adsorption kinetics were studied in detail and it was observed that the composite membrane showed synergistic improvement in dye adsorption. Such membranes can be used for water purification.

1. Introduction

Dyes used in textile industries are usually carcinogenic that can affect the reproductive system adversely [1] and exhibit neurotoxicity [2]. These dyes are released in water and cause water pollution [3, 4]. A variety of techniques has been developed for the removal of these dyes from wastewater [5]. These include adsorption, oxidation processes, electrochemical treatment, microbiological or enzymatic decomposition and decolorization by photocatalysis etc [6–9]. Magnetic nanoparticles are preferred for easy separation and recycling. Fe_3O_4 or Fe_2O_3 nanoparticles along with silver nanoparticles in a composite form have also been studied because of their adsorption as well as antibacterial properties [10–17]. Fe_3O_4 nanoparticles have been used for heavy metal adsorption as well from waste water treatment [18, 19]. Fe_2O_3 nanoparticles have also been studied for magnetic separation of dyes from wastewater [20]. Maghemite nanoparticles were used for removal of congo red dye in wastewater [21].

There are various chemical routes available for the synthesis of magnetic nanoparticles such as sol–gel reactions, decomposition of organometallic precursors, precipitation, high-temperature reactions, reactions in steric environments, polyol methods, etc [22]. The solution combustion method has been employed to synthesize highly crystalline oxide nanoparticles with uniform size and high surface area [23–25]. Combustion synthesized TiO_2 was found to be superior to commercial available catalysts for the degradation of various dyes and organic compounds [26–33]. In this study, the use of combustion synthesized metal oxide nanoparticles for adsorption of dyes [30, 34] has been explored.

PVDF [poly (vinylidene fluoride)] is extensively used as membranes because of its excellent properties such as inertness, high thermal and mechanical properties [35, 36]. In our recent work, we have attempted to prepare

porous PVDF membranes using crystallization induced phase separation as a tool [37]. Several procedures are available for the fabrication of PVDF membranes such as phase inversion, use of inorganic particles as a filler or as an additive, sintering, and track etching etc [36]. Among these techniques, non-solvent induced phase separation is the simplest and hence most widely used method for membrane fabrication.

In this present work, we have synthesized Fe based adsorbents using solution combustion and sol–gel techniques. The synthesized adsorbents were extensively characterized by different techniques including TEM, scanning electron microscopy (SEM), BET and XRD. Three cationic dyes were used for the adsorption studies. The equilibrium isotherm, adsorption kinetics has been systematically studied. Further, poly vinylidene (PVDF) composite membranes containing the synthesized nanoparticles were prepared via phase inversion technique. Membrane morphology was characterized using SEM for analyzing the pore size and distribution. The pure water flux was calculated for both neat PVDF and the composite membranes. The kinetics of adsorption were studied for both membranes and it was found that composite membrane shows synergistic improvement in dye adsorption.

2. Experimental section

2.1. Materials

Poly (vinylidene fluoride) PVDF (Kynar 761, M_w 440 000 g mol^{-1}) was purchased from Arkema Inc. Ferrous nitrate, urea and silver nitrate was obtained from SD Fine Chemicals, India. DMF and hydrazine hydrate were obtained from commercial sources and used as received without any further purification. All the dyes, malachite green (MG), methyl violet (MV) and pyronin Y (Py) were purchased from SD Fine Chemicals, India. All these dyes are cationic chlorinated dyes and belong to same structural group; MG with $\lambda_{max} = 617$ nm, MV with $\lambda_{max} = 584$ nm and Py with $\lambda_{max} = 546$ nm.

2.2. Synthesis of nanoparticles

2.2.1. Fe_2O_3 nanoparticles

Solution combustion technique was employed to synthesize iron (III) oxide (Fe_2O_3) nanoparticles. In the synthesis process, ferric nitrate nonahydrate ($Fe(NO_3)_3.9H_2O$) was dissolved in DI water and was used as an oxidizer for the combustion. Urea was dissolved in DI water and was used as fuel. The reaction based on stoichiometric (molar) ratio of oxidizer and fuel can be written as equation (1)

$$Fe(NO_3)_3.9H_2O + N_2H_4CO \rightarrow Fe_2O_3 + H_2O + CO_2 + N_2. \quad (1)$$

The stoichiometric amounts of oxidizer and fuel precursors were mixed and kept at 450 °C in a preheated furnace. The progress of reaction was continuously monitored until the solid product was formed. The obtained silver-gray product was grounded into fine powder before subjecting to further studies.

2.2.2. Fe_2O_3:Ag(C) nanoparticles using solution combustion method

Solution combustion technique was employed to synthesize the iron (III) oxide–silver (Fe_2O_3:Ag) nanoparticles. In this synthetic process, ferric nitrate nonahydrate ($Fe(NO_3)_3.9H_2O$) and silver nitrate were dissolved in DI water separately and were used as oxidizer for the combustion. Urea was dissolved in DI water separately and was used as fuel. Both fuel and oxidizer were mixed together and sonicated for 10 min to ensure proper mixing. The reaction based on oxidizer to fuel stoichiometric (molar) ratio can be written as equation (2)

$$Fe(NO_3)_3.9H_2O + AgNO_3 + N_2H_4CO \rightarrow Fe_2O_3: Ag + H_2O + CO_2 + N_2. \quad (2)$$

The stoichiometric amount of oxidizers and fuel precursors was mixed and kept at 450 °C in a preheated furnace. The progress of reaction was continuously monitored till the solid product was formed. The obtained silver-gray color product was grounded into fine powder before subjecting to further studies.

2.2.3. Fe_2O_3:Ag(S) nanoparticles using in situ reduction method

Fe_2O_3 nanoparticles, synthesized as mentioned above, using solution combustion was used to prepare Ag decorated Fe_2O_3 nanoparticles. Typically, Fe_2O_3 nanoparticles were dispersed in ethanol into which 0.005 M $AgNO_3$ solution was added and stirred for 1 h. Subsequently, hydrazine hydrate (as reducing agent) was added drop wise into solution and stirred for 12 h. The Fe_2O_3:Ag(S) was centrifuged, washed repeatedly with ethanol, and finally vacuum dried overnight.

2.3. Characterization

The microstructure of the adsorbents was evaluated using TEM (FEI F30) operated at 200 kV. TEM samples were prepared by dispersing the nanoparticles in ethanol using probe sonication. Samples were drop casted on a carbon coated copper grid. Powder XRD (PANalytical X'pert Pro) was carried out using a Cu Kα radiation (1.54 Å) at 40 k eV and at 30 mA. Zeta potential of adsorbents was measured (ZetaPals) in water at pH 7. Prior to

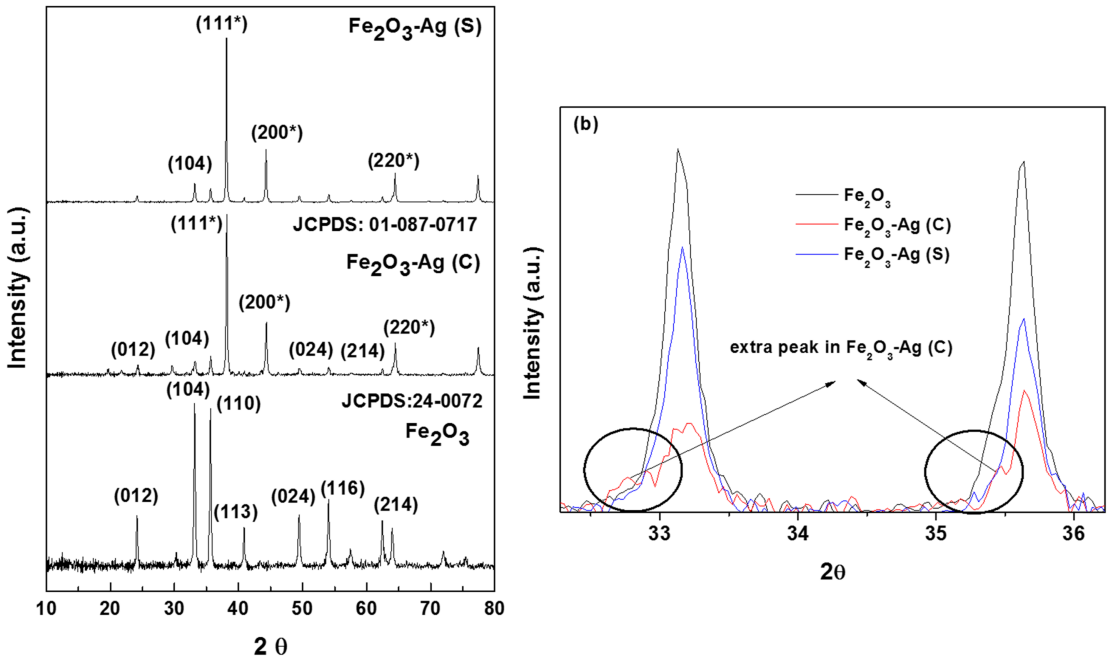

Figure 1. XRD scans for synthesized nanoparticles, (a) Fe_2O_3, Fe_2O_3–Ag(C), Fe_2O_3–Ag(S); (b) magnified scans of Fe_2O_3, Fe_2O_3–Ag(C) nanoparticles.

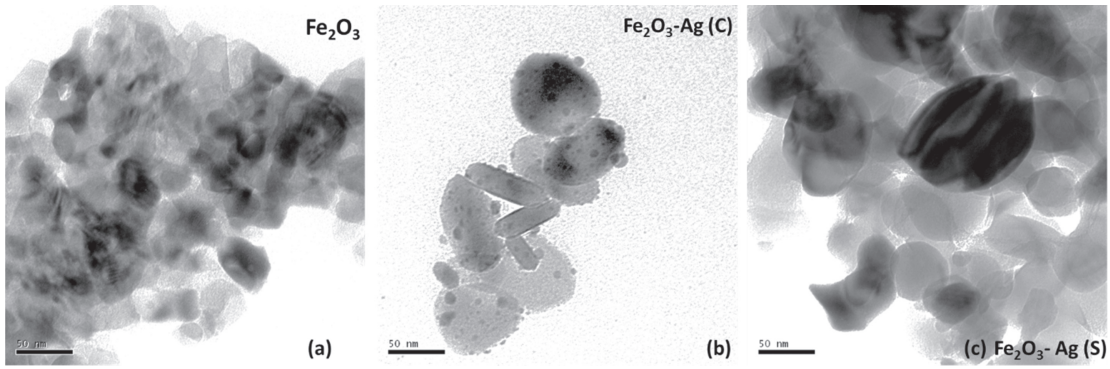

Figure 2. TEM micrographs of nanoparticles (a) Fe_2O_3, (b) Fe_2O_3–Ag(C) and (c) Fe_2O_3–Ag (S).

measurement, samples were dispersed in water (1 mg ml^{-1}) using bath sonication at its natural pH. For SEM imaging, the powder samples were dispersed in ethanol using sonication and drop casted onto silicon wafer. Ultra 55, Carl Zeiss, Germany equipped with EDAX was used to analyze the morphology, elemental mapping and analysis of adsorbents. The magnetization measurement of various adsorbents was obtained using vibrating sample magnetometer (Lakeshore, VSM). For surface area analysis, BET was performed using adsorption based on liquid nitrogen with a BET analyzer (Quantachrome).

2.4. Adsorption experiments

Adsorption experiments were carried out using all the three aforementioned with 10 ml of different dye solutions (MG, MV, Py) at different initial concentrations at 1 g l^{-1} adsorbent dosage. For each study, 10 ml of dye stock solution with adsorbent were taken in a beaker, covered with paraffin film and kept in incubator shaker at 37 °C at pH 7. The absorption spectra of dye solution before and after adsorption were recorded using plate reader (Biotek) at their respective wavelength. The concentration was measured at a characteristic wavelength using a calibrated curve based on Beer–Lambert's law for each dye.

2.5. Membrane preparation

PVDF membranes were prepared using the phase inversion method at 4 °C. A homogeneous 15 wt% PVDF solution in DMF was dispersed uniformly on a glass plate (ca 250 μm), and then precipitated in non-solvent

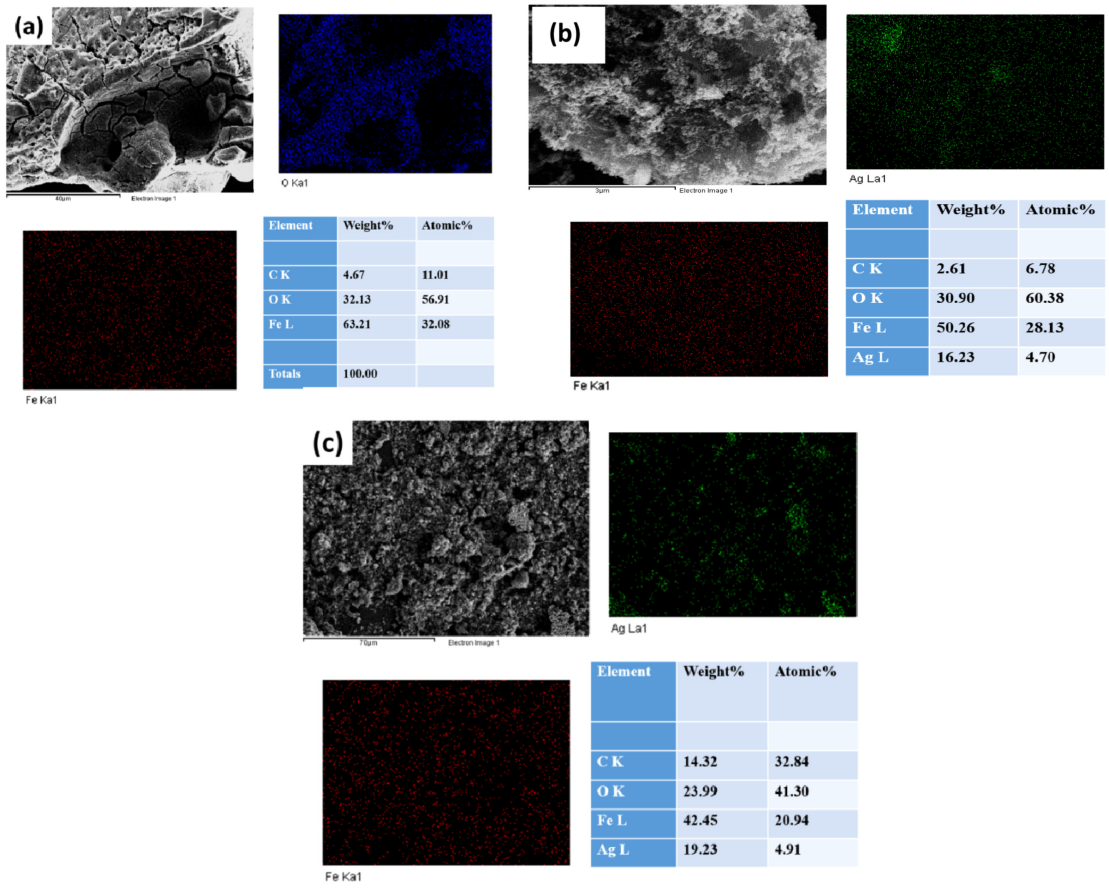

Element	Weight%	Atomic%
C K	4.67	11.01
O K	32.13	56.91
Fe L	63.21	32.08
Totals	100.00	

Element	Weight%	Atomic%
C K	2.61	6.78
O K	30.90	60.38
Fe L	50.26	28.13
Ag L	16.23	4.70

Element	Weight%	Atomic%
C K	14.32	32.84
O K	23.99	41.30
Fe L	42.45	20.94
Ag L	19.23	4.91

Figure 3. SEM and EDAX mapping of (a) Fe_2O_3, (b) Fe_2O_3–Ag (C) and (c) Fe_2O_3–Ag (S) nanoparticles. The elemental composition is shown in respective table for large area EDAX.

(water) to generate a porous membrane. The latter was dried at 45 °C for 12 h and then examined under a SEM (Carl Zeiss, Germany) for the obtained microstructure. For PVDF/Fe_2O_3:Ag membranes, the same protocol was adopted, i.e. homogeneous 15 wt% PVDF solution in DMF was prepared separately, Fe_2O_3:Ag nanoparticles were dispersed separately in DMF using probe sonication. Both particles and the PVDF solution were mixed together using a shear mixer at 8000 rpm for 45 min The solution was uniformly coated on a glass plate (ca 250 μm), and then precipitated in non-solvent (water) to generate a porous membrane. The latter was dried at 45 °C for 12 h to remove water and DMF.

2.6. Flux calculation

The water flux across the membranes was calculated using an in-house designed vertical crossflow cell setup. The retentate was continuously circulated whereas permeate was collected and used for flux calculations. All the experiments were done at 30 °C with DI water. Before measuring flux, porous membranes were stabilized for 1 h at 30 psi. For statistical analysis, three replicates of membranes were measured. The trans-membrane flux (J_w) was calculated using the following equation (3)

$$J_w = \frac{V}{Axt}. \tag{3}$$

In equation (3), A is the effective area of the membrane, V is the collected permeated, and t is the time taken to fill the volume (V).

3. Results and discussion

3.1. Characterization of the different adsorbents

The XRD spectra of Fe_2O_3 showed characteristic peaks that are consistent with the standard data of rhombohedral [38] α-Fe_2O_3 (JCPDS 24-0072), as shown in figure 1. The sharp and strong peaks of Fe_2O_3 indicate high crystallinity of the synthesized nanoparticles. The XRD patterns of Fe_2O_3:Ag(C) and Fe_2O_3:Ag(S)

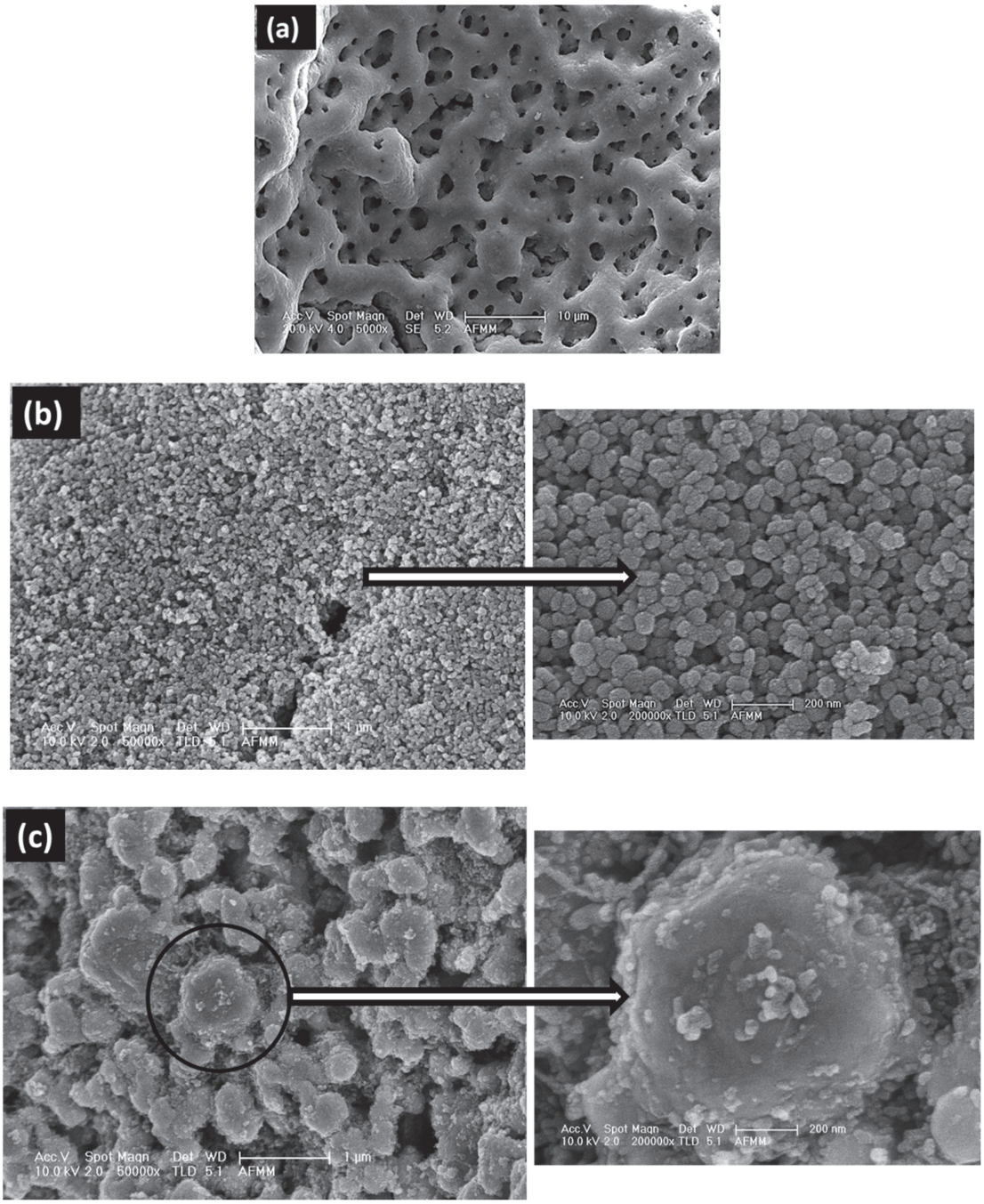

Figure 4. SEM morphology of (a) Fe_2O_3, (b) Fe_2O_3–Ag (C) and (c) Fe_2O_3–Ag (S) nanoparticles.

are also reported in figure 1(a). The XRD pattern of the particles indicated the formation of cubic silver lattice (111 at $2\theta = 38.1°$) (JCPDS 01-087-0717) in both. However, the lattice parameters for Fe_2O_3 in Fe_2O_3:Ag(C) is slightly different from Fe_2O_3. This is possibly due to the substitution of Ag in the Fe_2O_3 lattice during combustion synthesis that can increase the d-spacing of Fe_2O_3. Figure 1(b) shows the magnified region of characteristic peaks of α-Fe_2O_3 (104, 110). An extra peak was observed due to the existence of more than one phase of Fe_2O_3 with the addition of Ag during solution combustion method.

TEM studies of the adsorbents showed homogeneous crystallites of Fe_2O_3 (figure 2(a)). The TEM morphology of Fe_2O_3:Ag(C) is shown in figure 2(b). The small particles present on big Fe_2O_3 particles are Ag nanoparticles. The TEM–EDAX indicated the presence of Fe and Ag in the hybrid (not shown here). The TEM micrographs of Fe_2O_3:Ag(S) showed the Ag particles are attached onto the surface of Fe_2O_3. The average particle size of Ag on the surface of Fe_2O_3 was ca 50 nm (figure 2(c)). Figures 3(a)–(c) showed the SEM micrographs of synthesized adsorbents with EDAX mapping. The results indicated that the concentration of Ag is approximately similar in both the adsorbents (Fe_2O_3:Ag(C) and Fe_2O_3:Ag(S). This confirms the presence of

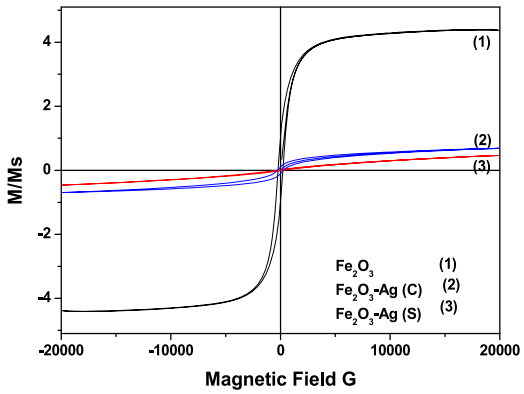

Figure 5. Vibrating sample magnetometer (VSM) hysteresis loop for Fe_2O_3, Fe_2O_3–Ag (C) and Fe_2O_3–Ag (S) nanoparticles.

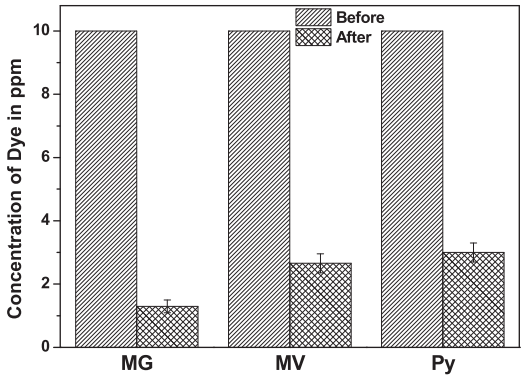

Figure 6. Concentration of different dyes left in solution (in ppm) after 12 h adsorption using Ag nanoparticles as adsorbent.

slightly higher Ag concentration in Fe_2O_3:Ag(S) as compared to Fe_2O_3:Ag(C) (figure 3). Moreover, from EDAX mapping, uniform distribution of Ag and Fe_2O_3 was observed in both the samples. The Fe_2O_3 particles show microporous morphology (figure 4). The morphology of Fe_2O_3:Ag(C) and Fe_2O_3:Ag(S) was different from Fe_2O_3 particles. At higher magnification, these particles appeared more porous than Fe_2O_3. The higher magnification showed that the porous structure could be agglomerated nanoparticles of Ag and Fe_2O_3. The morphology and size of particles was in accordance with the TEM images (figure 4). In Fe_2O_3:Ag (S), an interconnected network of pores was observed, which can help in better adsorption properties of these particles. Kwon *et al* [39] showed similar micrographs and explained the formation of macroporous α-Fe_2O_3 by Ostwald ripening during heat treatment.

Figure 5 shows the typical hysteresis loop for Fe_2O_3, Fe_2O_3:Ag(C), Fe_2O_3:Ag(S) powder obtained at 30 °C using magnetic field of 2 T. All the particles showed magnetic property. The saturation magnetization was maximum for Fe_2O_3 and the magnetization decreases with the addition of Ag in both Fe_2O_3: Ag(C), Fe_2O_3: Ag(S) particles. This indicated the presence of non-magnetic Ag on the surface of Fe_2O_3. As observed from figure 5, the saturated magnetization (M_s) of bare magnetic nanoparticles is 5 emu g^{-1}, while it decreased to 0.6 emu g^{-1} for the Fe_2O_3:Ag(C), Fe_2O_3:Ag(S) adsorbents. The decrease in M_s is because of the Ag coating on the surface of Fe_2O_3 that results in the quenching of surface moments [40].

The BET surface areas of nanoparticles were 17 m^2 g^{-1}, 27 m^2 g^{-1} and 31 m^2 g^{-1} for Fe_2O_3, Fe_2O_3:Ag(C) and Fe_2O_3:Ag(S) adsorbents, respectively. The surface areas of both the combustion synthesized and *in situ* synthesized materials were observed to be higher than Fe_2O_3 nanoparticles. However, from the SEM analysis, we found that solution combustion synthesized adsorbents were highly porous [34] (figure 4). Zeta potential (ξ) was used to evaluate the surface charge properties of the different adsorbents. For the Fe_2O_3 nanoparticles, ξ is −6 mV [41] which is lower than −30 mV for pH ~7, and higher than 30 mV suggesting a lack of stability of colloidal solution in the range of experimental pH. Fe_2O_3:Ag(C) and Fe_2O_3:Ag(S) show ξ of 11.1 and 23.9 mV, respectively. The addition of Ag changes the zeta potential of particles. This is due to the presence of Ag ions on the Fe_2O_3 particle surface, which changes the surface charge of the particles at neutral pH.

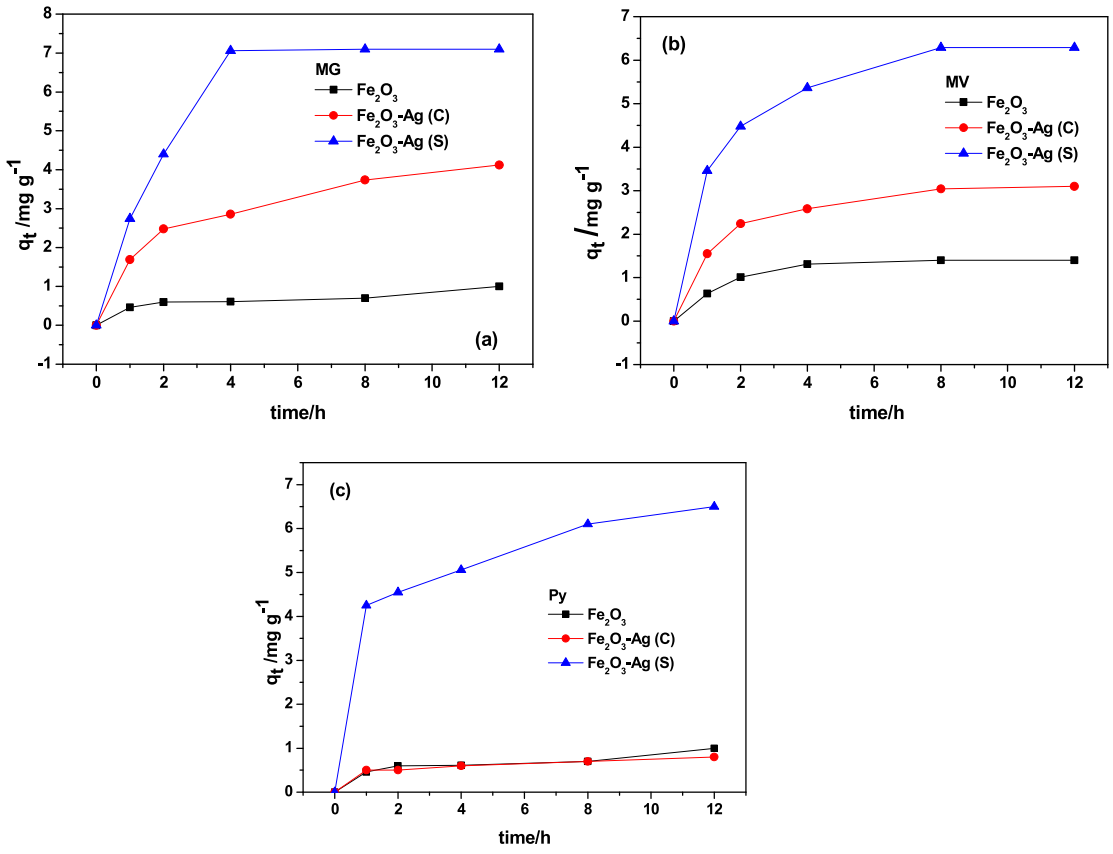

Figure 7. Variation of dyes uptake with time at natural pH (a) malachite green, (b) methyl violet and (c) pyronin Y using different adsorbents.

3.2. Adsorption studies

The toxicological effects of MG have been reported in literature [42–44] and it is acutely toxic to a wide range of aquatic and terrestrial life. Methyl violet also has toxic effects that may cause severe skin/eye irritation and can also infect the gastrointestinal tract [45–47]. Pyronin Y has been known to be cytostatic and cytotoxic to mitochondrial localization of the dye and its interaction with RNA [48]. The efficiency of adsorption of adsorbate mainly depends on the surface area and size distribution. In this study, Fe_2O_3:Ag based adsorbent with porous surface and nanosize distribution of particles in the presence of Fe and Ag may have a high sorption capacity. To understand the sorption mechanism, the kinetics and equilibrium of adsorption modeling was investigated.

The experimental procedure of adsorption is mentioned in experimental section. Before going into detail of Fe_2O_3 based adsorbents, it is worth mentioning that Ag nanoparticles are reported to be good adsorbents for synthetic dyes [49–51]. Figure 6 illustrates the concentration of all the three dyes remaining in the solution after sorption onto Ag nanoparticles. It is clear that Ag nanoparticles efficiently adsorb the dyes under investigation.

As both Ag and Fe_2O_3 showed adsorption of dyes, our main objective was to design a composite that can show synergistic effects and also have magnetism. To fulfill this, we synthesized Fe_2O_3:Ag composites using two different techniques in which Ag concentration was kept lower than Fe_2O_3. The idea of incorporating Fe_2O_3 in the composite is to impart magnetic properties to the composite that will be helpful in retrieving particles after sorption [52, 53].

3.2.1. Adsorption kinetics

To analyze the kinetics of adsorption, a pseudo second order kinetic model was used such that the concentration in the liquid phase is constant after the equilibrium is reached. This model proposes that the chemisorption is the rate-limiting step and the adsorption occurs on localized sites [6, 34]

$$\frac{dq_t}{dt} = k_2 (q_e - q_t)^2. \quad (4)$$

k_2 is the pseudo-second order rate constant for adsorption (g mg^{-1} min^{-1}) and q_e is the amount of dye adsorbed at equilibrium

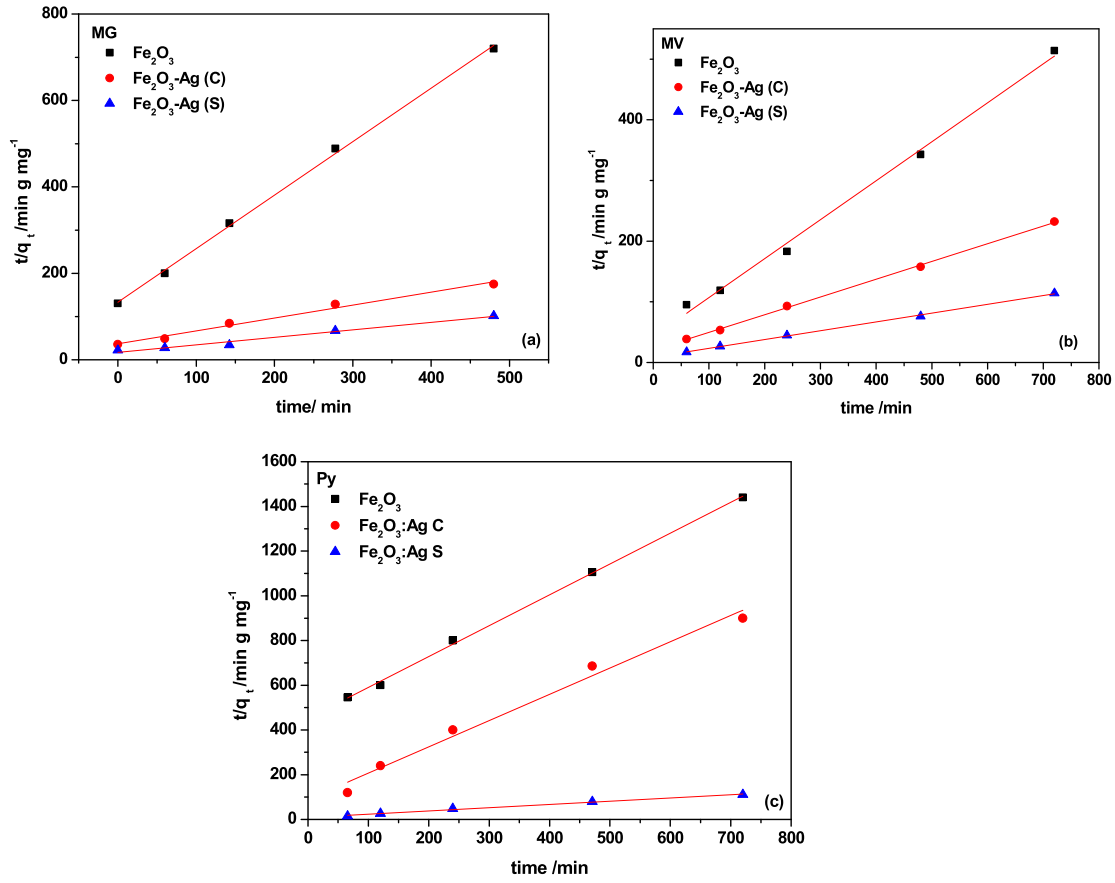

Figure 8. Pseudo second order kinetics fitting for (a) malachite green, (b) methyl violet and (c) pyronin Y using different adsorbents. Red lines indicate the fitting.

Table 1. Parameters obtained by fitting pseudo-second order kinetics, equilibrium concentration, and second order rate constant for all dyes with three adsorbents.

Adsorbent	q_e (mg g^{-1})	$k_2 q_e^2$ (g mg^{-1} min^{-1})
Malachite green		
Fe_2O_3	1.15	8.76×10^{-3}
Fe_2O_3–Ag(C)	4.75	0.0383
Fe_2O_3–Ag(S)	8.20	0.0913
Methyl violet		
Fe_2O_3	1.55	0.023
Fe_2O_3–Ag(C)	3.41	0.049
Fe_2O_3–Ag(S)	6.89	0.118
Pyronin Y		
Fe_2O_3	0.806	2.03×10^{-3}
Fe_2O_3–Ag(C)	0.857	0.0109
Fe_2O_3–Ag(S)	6.957	0.112

$$q_e = (C_o - C_e)V/W. \tag{5}$$

C_o and C_e are initial and equilibrium dye concentrations respectively, in mg l^{-1}. V is the volume of the dye solution used for adsorption in ml and W is the weight of adsorbent used for adsorption in g. q_t is the amount of dye adsorbed at any time t. By solving equation (4)

$$\frac{t}{q_t} = \frac{1}{q_e^2\, k_2} + \frac{1}{q_e} t. \tag{6}$$

Figures 7(a)–(c) show the variation in the amount of dye adsorbed (MG, MV and Py) on different adsorbents respectively, with time. In all cases, the equilibrium has reached in ~5–6 h. Figure 8 shows the variation of t/q_t

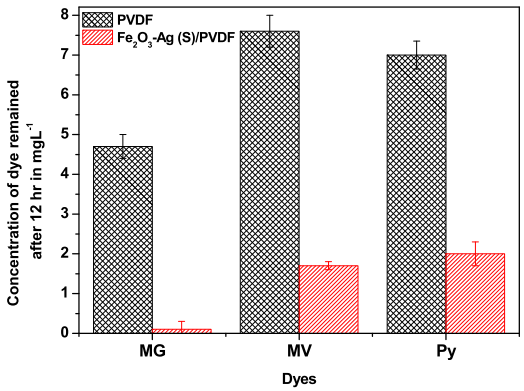

Figure 9. Concentration of different dyes left in solution (in ppm) after 12 h adsorption using neat PVDF and PVDF/Fe_2O_3–Ag (S) membranes as adsorbent.

Table 2. Parameters obtained by fitting pseudo-second order kinetics, for all dyes using PVDF and PVDF+ Fe_2O_3–Ag(S) adsorbent membranes.

Adsorbent	q_e (mg g^{-1})	$k_2 q_e^{\,2}$ (g mg^{-1} min^{-1})
Malachite green		
PVDF	7	0.056
PVDF + Fe_2O_3–Ag(S)	10	0.1848
Methyl violet		
PVDF	3	0.0528
PVDF + Fe_2O_3–Ag(S)	8.8	0.1760
Pyronin Y		
PVDF	3.12	0.0228
PVDF + Fe_2O_3–Ag(S)	8.9	0.0507

with time (t) for all dyes. The values of k_2 and q_e were calculated from the slope and intercept of the plots. The values of k_2 and q_e for all samples are presented in table 1. From figures 7 and 8, the amount of dye adsorbed at equilibrium (q_e) can be evaluated and was observed to be maximum for Fe_2O_3:Ag(S) for all the studied dyes. The initial adsorption rate is given as $k_2 q_e^{\,2}$. From table 1, the initial sorption rate was found to be maximum for Fe_2O_3:Ag(S) followed by Fe_2O_3:Ag(C) and Fe_2O_3. This is because Fe_2O_3:Ag(S) had higher dye uptake at equilibrium (q_e). The initial sorption rates of MG and MV were considerably higher than Py. These results suggest that adsorption takes place through a chemical process in which the valence forces proceed through sharing or exchanging electrons between the cationic dyes and the Fe_2O_3:Ag(S) nanocomposites [40, 54].

Similar to nanoparticles, we extend our dye adsorption kinetics to PVDF membranes. The dye adsorption properties of both neat and Fe_2O_3–Ag (S)/PVDF membranes were tested using all three dye adsorption studies. Figure 9 illustrates the amount of dye that remained in solution after 12 h. It is interesting to observe that Fe_2O_3–Ag (S)/PVDF membranes adsorbs more than neat PVDF membranes for all dyes. This can be attributed to presence of adsorbents (Fe_2O_3–Ag (S)) in the composite membranes. SEM micrographs of composite membrane morphology indicates that nanoparticles are agglomerated on membrane surface. Neat PVDF membrane also adsorb dyes due to the negative charge present on PVDF that is due to CF_2 groups and positively charged cationic dyes. The opposite charge interaction can lead to adsorption of cationic dyes onto PVDF surface.

Using equations (4)–(6), we calculated adsorption kinetics parameters (K_2 $q_e^{\,2}$ and q_e) for PVDF and Fe_2O_3–Ag (S)/PVDF membranes. The adsorption kinetics parameters are reported in table 2. As indicated from both figure 10 and table 2, the amount of dye adsorbed at equilibrium (q_e) is maximum for Fe_2O_3–Ag (S)/PVDF membranes for all dyes. The maximum dye adsorption was for MG. Similar to other polymers [55], PVDF is known for adsorbing organic dyes by attractive van der Waals interactions, hydrogen bonding and/or ion type [56]. Here, the synergistic effect from both PVDF and Fe_2O_3–Ag (S) nanoparticles help in dye adsorption to a higher extent. For instance, for MV and Py, Fe_2O_3–Ag (S) nanoparticles have an equilibrium dye uptake (q_e) of 6.8 and 6.9 mg g^{-1}, respectively. However, after incorporating into PVDF, the equilibrium dye uptake (q_e) increased to 8.8 and 8.9 mg g^{-1} respectively with 25 wt% nanoparticle concentration.

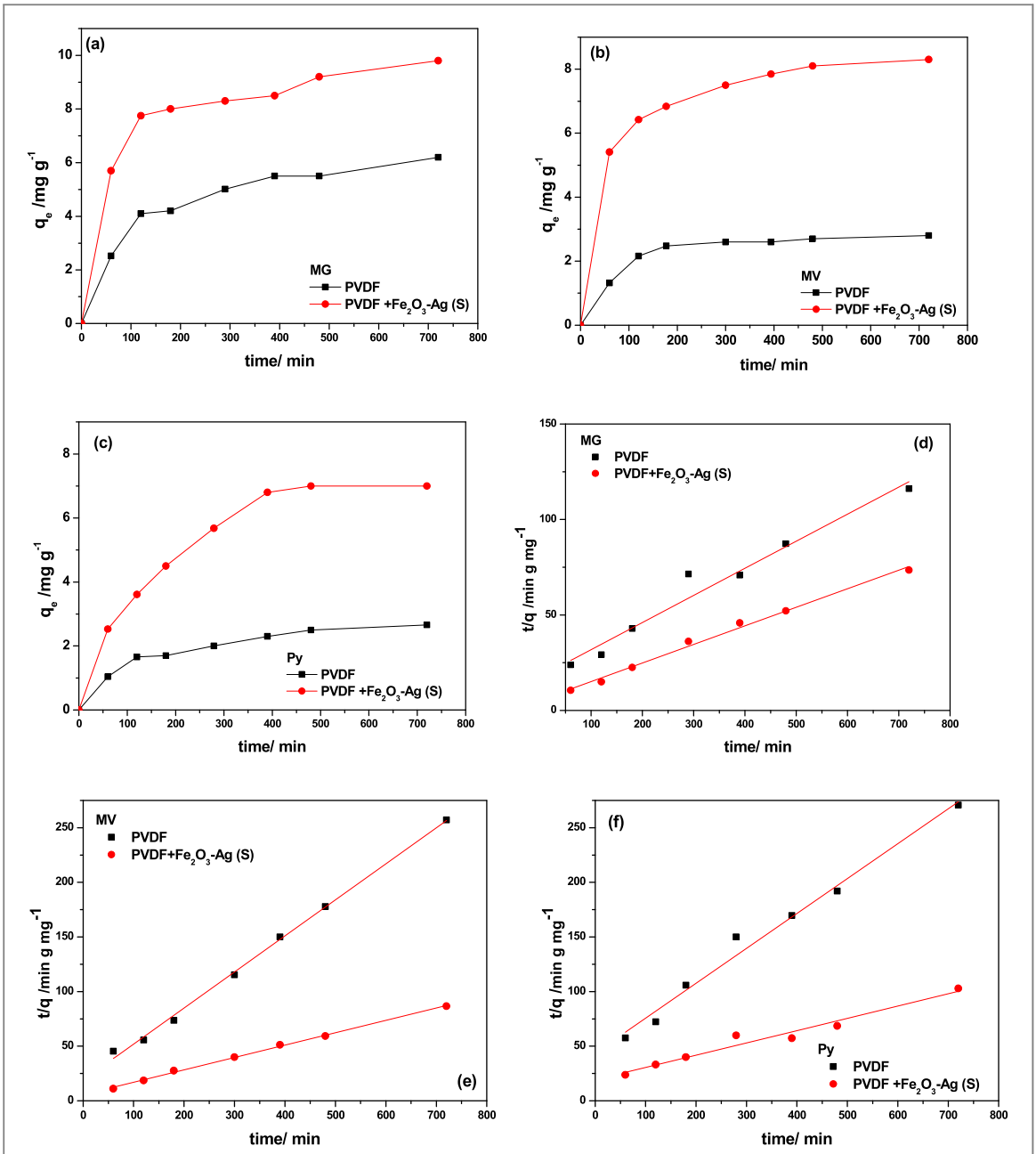

Figure 10. Variation of dyes uptake with time at natural pH (a) malachite green, (b) methyl violet and (c) pyronin Y using both neat PVDF and PVDF/Fe_2O_3–Ag (S) membranes. Pseudo second order kinetics fitting for (d) malachite green, (e) methyl violet and (f) pyronin Y using different adsorbents. Red lines indicate the fitting.

3.3. Equilibrium isotherms

Equilibrium isotherm studies are used to predict the interaction between adsorbent and adsorbate at a given condition and obtain the maximum adsorption capacity of the adsorbent. Langmuir and Freundlich are the widely accepted models for sorption process. Langmuir isotherm assumes monolayer adsorption of dye molecules on uniform sites of adsorbent with equal binding energy [57]. The equation is;

$$q_e = q_m \frac{K_1 C_e}{1 + K_1 C_e}. \tag{7}$$

This can be linearized as

$$\frac{c_e}{q_e} = \frac{c_e}{q_m} + \frac{1}{q_m K_s}. \tag{8}$$

In equation (8), q_e is the amount of dye adsorbed at equilibrium per unit weight of adsorbent (mg g^{-1}), c_e is the dye concentration at equilibrium (mg l^{-1}), q_m is the maximum amount of dye adsorbed at equilibrium per unit weight of adsorbent (mg g^{-1}) and K_s is the Langmuir adsorption constant (l mg^{-1}). The Langmuir isotherms for

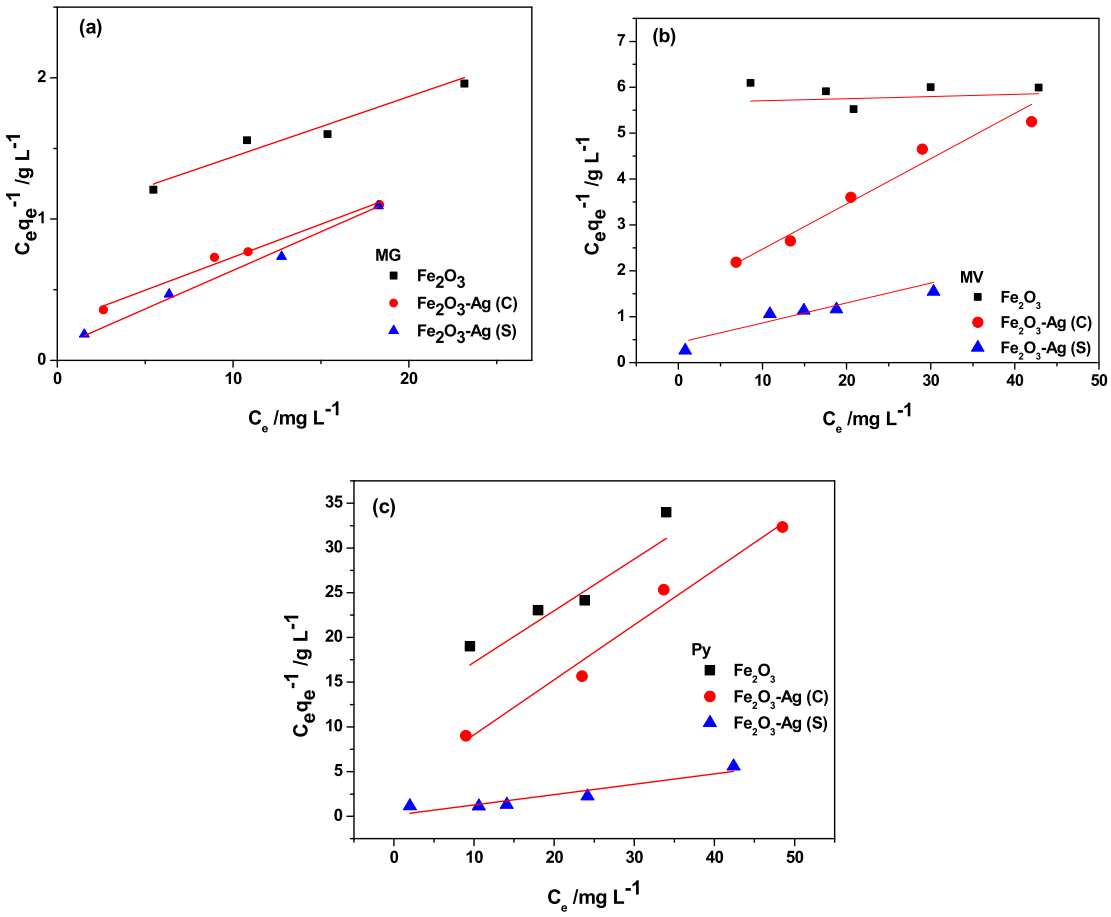

Figure 11. The variation of equilibrium uptake of different dyes (a) malachite green, (b) methyl violet and (c) pyronin Y using different adsorbents at natural pH and room temperature. Solid lines indicate the Langmuir model for the adsorption.

Table 3. Parameters obtained by fitting equilibrium isotherm for all dyes with three adsorbents.

Adsorbent	K_s (l mg^{-1})		K_s (l mg^{-1})		K_s (l mg^{-1})
Malachite Green		Methyl violet		Pyronin Y	
Fe_2O_3	0.010	Fe_2O_3	0.042	Fe_2O_3	0.05
Fe_2O_3–Ag(C)	0.10	Fe_2O_3:Ag S	0.60	Fe_2O_3:Ag C	1.05
Fe_2O_3–Ag(S)	0.06	Fe_2O_3:Ag C	0.17	Fe_2O_3:Ag S	0.2

adsorption of all dyes on three adsorbents are shown in figure 11. The adsorption parameters i.e. q_m and K_s were obtained from the slope and intercept of the plot of c_e/q_e with c_e plot based on equation (8), respectively. The solid lines represent the pseudo second order fitting to the experimental data. The values of K_s and q_m for all samples are presented in table 3. As indicated in table 3, the equilibrium adsorption constant was the maximum for Fe_2O_3:Ag (S) particles for all dyes. From the values of equilibrium adsorption studies, the adsorption capacity follows the order Fe_2O_3 < Fe_2O_3:Ag(C) < Fe_2O_3:Ag(S).

3.4. Mechanism of dye adsorption

The key factors for sorption of any dye on adsorbent are surface characteristics, size distribution and extent of functional groups present in an adsorbent. Here in this work, the electrostatic attraction between cationic dyes and Fe_2O_3 nanoparticles [40] and also the interaction between the Lewis base –$N(CH_3)_2$ in chlorinated cationic dyes and the water molecule coordinated Fe_2O_3 nanoparticles [58] can lead to adsorption of dyes on adsorbent surface. Apart from Fe_2O_3, Ag nanoparticles are also known to adsorb cationic dyes [50]. Fe_2O_3:Ag(C) and Fe_2O_3:Ag(S) nanoparticles showed high adsorption than Fe_2O_3. This can be attributed to the synergistic effects from both Fe_2O_3 and Ag nanoparticles. Among Fe_2O_3:Ag(C) and Fe_2O_3:Ag(S) nanoparticles, the latter showed better adsorption properties that can also be attributed to high Ag/Fe ratio in Fe_2O_3:Ag(S) nanoparticles than Fe_2O_3:Ag(C) nanoparticles. The BET surface area studies indicated the high surface area for Fe_2O_3:Ag S

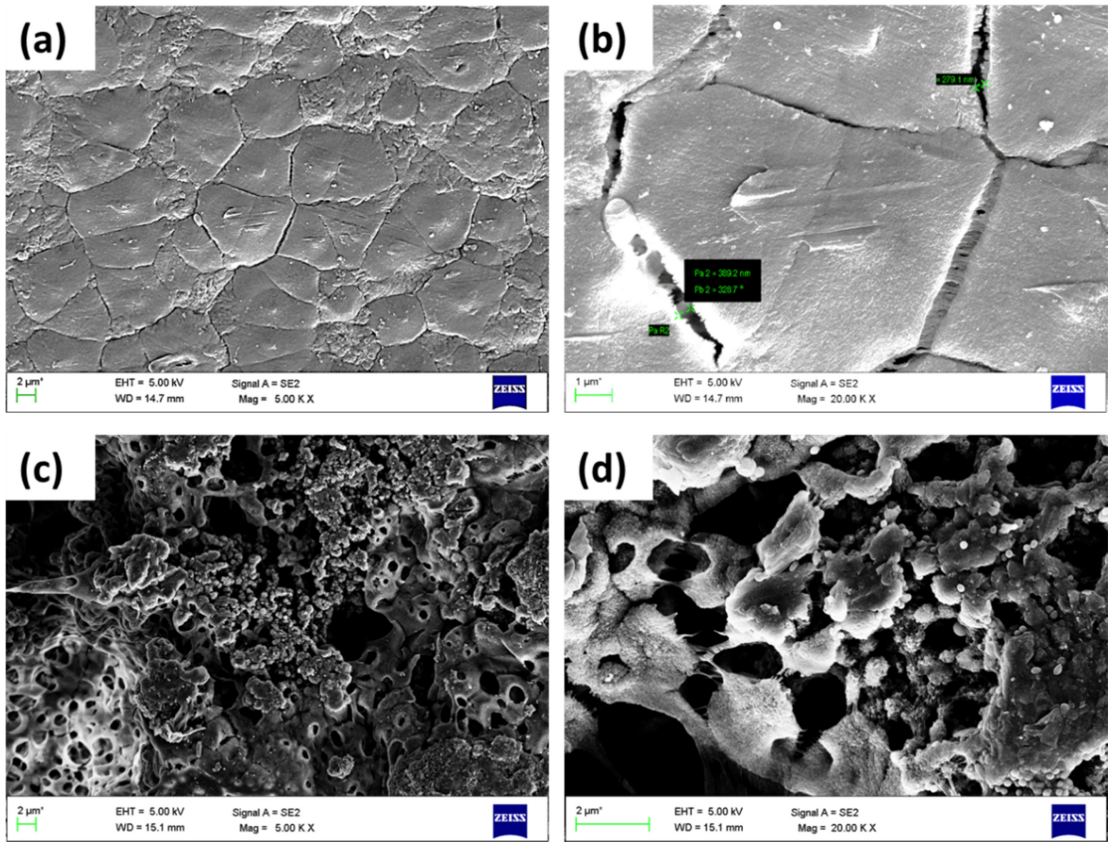

Figure 12. SEM micrographs of top surface (a) neat PVDF, (c) PVDF/Fe_2O_3–Ag (S) porous membranes. (b) and (d) Indicates the magnified images of PVDF and PVDF/Fe_2O_3–Ag (S) membranes, respectively.

adsorbents. The high surface area and slight high Ag content in Fe_2O_3:Ag(S) adsorbent can make these particles better adsorbents.

3.5. Morphology and flux determination of membranes

From the above studies, it is clear that Fe_2O_3:Ag(S) nanoparticles were better than the remaining nanoparticles studied. Fe_2O_3:Ag(S) nanoparticles proved as good adsorbents for all the three dyes. Taking this into consideration, we used Fe_2O_3:Ag(S) nanoparticles for further studies and prepared Fe_2O_3:Ag(S)/PVDF porous membranes via phase inversion method. The SEM images of the top surface of both the membranes (neat PVDF and Fe_2O_3:Ag S/PVDF) prepared are shown in figures 12(a)–(d). Crystalline morphology (spherulites) were clearly visible in the SEM images of neat PVDF (figure 12(a)). In the magnified images of membrane (figure 12(b)), the black lines are the connecting pores. The average size of these channels obtained from SEM is ca 200–300 nm. Figures 12(c) and (d) showed the representative morphology of the membranes with Fe_2O_3:Ag (S) at two different magnifications. In figure 12(c), the agglomerated nanoparticles on the surface of membranes can be observed. The average pore size becomes higher after addition of nanoparticles because of the fast crystallization in the presence of external particles and the overall connectivity of the pores increases [59]. However, the agglomerated structures can decrease the overall flux of the membranes as the concentration of nanoparticles is very high in modified membranes. It has been reported that at high TiO_2 dosage, agglomeration of TiO_2 particles in PVDF matrix restrained the formation of spherulites and led to less pores and lower porosity in hybrid membrane [60]. Similar results were obtained [61] in which the size of the pores increases after addition of Ag/MWNTs in PVDF matrix. The final morphology of the crystallites was dependent on the kinetics of nucleation and growth [60]. The crystal nuclei is formed by homogeneous nucleation in the absence of any foreign nucleating agent but heterogeneous nucleation occurs in the presence of nucleating agent (here Fe_2O_3: Ag(S)).

Trans-membrane flux for all samples at different pressures was obtained using equation (3) and is plotted in figure 13(a) and the flux at a particular pressure (15 psi) is shown in figure 13(b). The effect of nanoparticles on the PVDF membrane on the pure water permeability of membranes is shown in figure 13. It is evident that addition of Fe_2O_3:Ag(S) nanoparticles in PVDF membranes significantly decreased the water flux through the

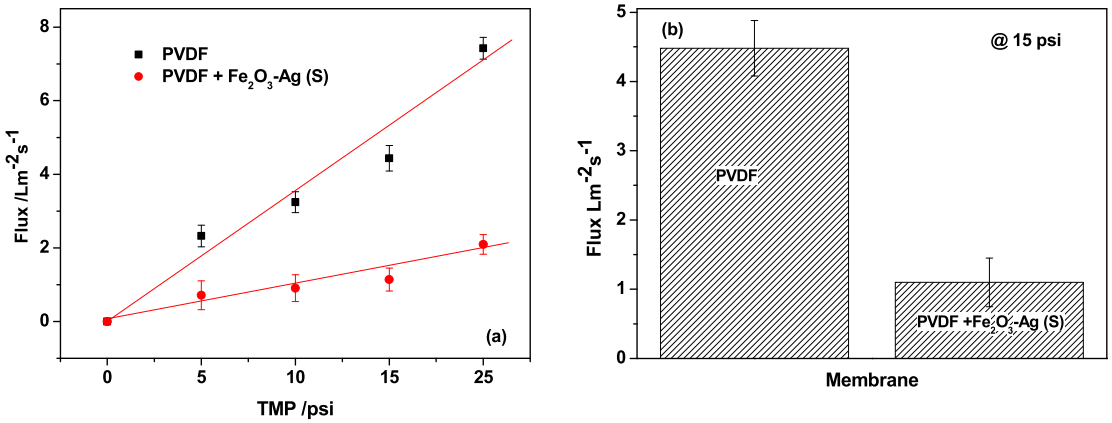

Figure 13. Transmembrane water flux calculation for both neat PVDF and PVDF/Fe_2O_3–Ag (S) membranes (a), flux through membranes at 15 psi (b).

membranes. The pure water flux across different membranes was much higher than those reported earlier fabricated using the conventional methods [62, 63]. This can be attributed to the presence of agglomerated nanoparticles in the membrane that can decrease the water porosity through the membrane. Similar results were reported in literature where addition of nanofillers beyond a specific concentration decreases the water flux in membranes [64, 65].

4. Conclusions

In this work, we have synthesized Fe (iron) and Ag (silver) based adsorbents using solution combustion and by sol gel technique. The synthesized adsorbents were characterized in detail by different techniques including electron microscopy, BET, XRD, Zeta potential etc. In order to study the adsorption kinetics and isotherms, three chlorinated cationic dyes (MG, MV and Py) were used on various synthesized adsorbents such as [iron III oxide (Fe_2O_3)], iron III oxide decorated silver nanoparticles by combustion synthesis technique [Fe_2O_3–Ag(C)] and iron III oxide decorated silver nanoparticles by *in situ* reduction technique, [Fe_2O_3–Ag (S)]. All the adsorbents followed pseudo-second-order kinetics model and the adsorption equilibrium was found to follow Langmuir adsorption. Among three synthesized adsorbents, Fe_2O_3–Ag(S) nanoparticles showed the maximum adsorption and is attributed to their high surface area. Poly vinylidene fluoride (PVDF) based membranes containing Fe_2O_3–Ag(S) nanoparticles were prepared via phase inversion (precipitation immersion using DMF/water) technique. The adsorption kinetics was further carried out with the composite membrane and the composite membrane showed synergistic improvement in dye adsorption for all three dyes. Such membranes can provide new pathways in water purification as they can adsorb cationic dyes as well as can prevent biofouling.

Acknowledgments

The authors thankfully acknowledge Department of Science and Technology (DST), India for financial support. Authors are also like to acknowledge Prof S Subramanian, Department of Chemical Engineering, IISc, for extending his Zeta potential and BET surface area analysis facilities. Authors acknowledge MNCF, CeNSe IISc, for characterization facilities. Giridhar Madras thanks DST for the J C Bose fellowship.

References

[1] Rachootin P and Olsen J 1983 *J. Occup. Environ. Med.* **25** 394–402
[2] Soni P, Sharma S, Sharma S, Kumar S and Sharma K P 2006 *J. Environ. Biol./Acad. Environ. Biol. India* **27** 623–8
[3] Kant R 2012 *Nat. Sci.* **4** 5
[4] Forgacs E, Cserháti T and Oros G 2004 *Environ. Int.* **30** 953–71
[5] Hao O J, Kim H and Chiang P-C 2000 *Crit. Rev. Environ. Sci. Technol.* **30** 449–505
[6] Konaganti V K, Kota R, Patil S and Madras G 2010 *Chem. Eng. J.* **158** 393–401
[7] Tünay O, Kabdasli I, Eremektar G and Orhon D 1996 *Water Sci. Technol.* **34** 9–16
[8] Slokar Y M and Le Marechal A M 1998 *Dyes Pigm.* **37** 335–56
[9] Naumczyk J, Szpyrkowicz L and Zilio-Grandi F 1996 *Water Sci. Technol.* **34** 17–24

[10] Zhai Y, Han L, Wang P, Li G, Ren W, Liu L, Wang E and Dong S 2011 *ACS Nano* **5** 8562–70
[11] Park H H, Park S, Ko G and Woo K 2013 *J. Mater. Chem.* B **1** 2701–9
[12] Liu J, Zhao Z, Feng H and Cui F 2012 *J. Mater. Chem.* **22** 13891–4
[13] Zhang X, Niu H, Yan J and Cai Y 2011 *Colloids Surf.* A **375** 186–92
[14] Wei Z, Zhou Z, Yang M, Lin C, Zhao Z, Huang D, Chen Z and Gao J 2011 *J. Mater. Chem.* **21** 16344–8
[15] Prucek R, Tuček J, Kilianová M, Panáček A, Kvítek L, Filip J, Kolář M, Tománková K and Zbořil R 2011 *Biomaterials* **32** 4704–13
[16] Ping G, Huimin L, Xiaoxiao H, Kemin W, Jianbing H, Weihong T, Shouchun Z and Xiaohai Y 2007 *Nanotechnology* **18** 285604
[17] Gao N, Chen Y and Jiang J 2013 *ACS Appl. Mater. Interfaces* **5** 11307–14
[18] Bhunia P, Kim G, Baik C and Lee H 2012 *Chem. Commun.* **48** 9888–90
[19] Liu Y, Zhou L, Hu Y, Guo C, Qian H, Zhang F and Lou X W 2011 *J. Mater. Chem.* **21** 18359–64
[20] Qu S, Huang F, Yu S, Chen G and Kong J 2008 *J. Hazard. Mater.* **160** 643–7
[21] Afkhami A and Moosavi R 2010 *J. Hazard. Mater.* **174** 398–403
[22] Laurent S, Forge D, Port M, Roch A, Robic C, Vander Elst L and Muller R N 2008 *Chem. Rev.* **108** 2064–110
[23] Patil K C, Aruna S T and Mimani T 2002 *Curr. Opin. Solid State Mater. Sci.* **6** 507–12
[24] Aruna S T and Mukasyan A S 2008 *Curr. Opin. Solid State Mater. Sci.* **12** 44–50
[25] Rajeshwar K and de Tacconi N R 2009 *Chem. Soc. Rev.* **38** 1984–98
[26] Sivalingam G, Nagaveni K, Hegde M S and Madras G 2003 *Appl. Catal.* B **45** 23–38
[27] Nagaveni K, Hegde M S, Ravishankar N, Subbanna G N and Madras G 2004 *Langmuir* **20** 2900–7
[28] Aarthi T and Madras G 2008 *Catal. Commun.* **9** 630–4
[29] Priya M H and Madras G 2006 *J. Photochem. Photobiol.* A **178** 1–7
[30] Aarthi T, Narahari P and Madras G 2007 *J. Hazard. Mater.* **149** 725–34
[31] Nagaveni K, Hegde M S and Madras G 2004 *J. Phys. Chem.* B **108** 20204–12
[32] Nagaveni K, Sivalingam G, Hegde M S and Madras G 2004 *Appl. Catal.* B **48** 83–93
[33] Nagaveni K, Sivalingam G, Hegde M S and Madras G 2004 *Environ. Sci. Technol.* **38** 1600–4
[34] Shukla R and Madras G 2014 *J. Environ. Chem. Eng.* **2** 2259–68
[35] Gopal R, Kaur S, Feng C Y, Chan C, Ramakrishna S, Tabe S and Matsuura T 2007 *J. Membr. Sci.* **289** 210–9
[36] Liu F, Hashim N A, Liu Y, Abed M R M and Li K 2011 *J. Membr. Sci.* **375** 1–27
[37] Sharma M, Madras G and Bose S 2015 *J. Mater. Chem.* A **3** 5991–6003
[38] Liu Z, Lv B, Wu D, Sun Y and Xu Y 2013 *Particuology* **11** 327–33
[39] Kwon K-A, Lim H-S, Sun Y-K and Suh K-D 2014 *J. Phys. Chem.* C **118** 2897–907
[40] Lakouraj M M, Norouzian R-S and Balo S 2015 *J. Chem. Eng. Data* **60** 2262–72
[41] Taboada E, Rodriguez E, Roig A, Oró J, Roch A and Muller R N 2007 **23** 4583–8
[42] Srivastava S, Sinha R and Roy D 2004 *Aquat. Toxicol.* **66** 319–29
[43] Fernandes C, Lalitha V S and Rao K V K 1991 *Carcinogenesis* **12** 839–45
[44] Rao K V K 1995 *Toxicol. Lett.* **81** 107–13
[45] Mittal A, Gajbe V and Mittal J 2008 *J. Hazard. Mater.* **150** 364–75
[46] Liu R, Zhang B, Mei D, Zhang H and Liu J 2011 *Desalination* **268** 111–6
[47] Rahchamani J, Mousavi H Z and Behzad M 2011 *Desalination* **267** 256–60
[48] Darzynkiewicz Z, Kapuscinski J, Carter S P, Schmid F A and Melamed M R 1986 *Cancer Res.* **46** 5760–6
[49] Pal J and Deb M 2014 *Appl. Nanosci.* **4** 967–78
[50] Femila E E, Srimathi R and Deivasigamani C 2014 *Int. J. Pharm. Pharm. Sci.* **6** 579–83
[51] Pal J, Deb M, Deshmukh D and Verma D 2013 *Appl. Water Sci.* **3** 367–74
[52] Tan K A, Morad N, Teng T T, Norli I and Panneerselvam P 2012 *APCBEE Proc.* **1** 83–9
[53] Yang N, Zhu S, Zhang D and Xu S 2008 *Mater. Lett.* **62** 645–7
[54] Chaudhary G R, Saharan P, Kumar A, Mehta S K, Mor S and Umar A 2013 *J. Nanosci. Nanotechnol.* **13** 3240–5
[55] Mahanta D, Madras G, Radhakrishnan S and Patil S 2008 *J. Phys. Chem.* B **112** 10153–7
[56] Alaoui O T, Nguyen Q T, Schaetzel P and Mbareck C 2011 *Catal. Sci. Technol.* **1** 1412–22
[57] Singh S A, Vemparala B and Madras G 2015 *J. Environ. Chem. Eng.* **3** 2684–96
[58] Huo S-H and Yan X-P 2012 *J. Mater. Chem.* **22** 7449–55
[59] Teow Y H, Ahmad A L, Lim J K and Ooi B S 2012 *Desalination* **295** 61–9
[60] Shi F, Ma Y, Ma J, Wang P and Sun W 2012 *J. Membr. Sci.* **389** 522–31
[61] He L, Yao L, Sun J, Wang X, Song R, He Y and Huang W 2012 *RSC Adv.* **2** 1516–23
[62] Nunes S P and Peinemann K V 1992 *J. Membr. Sci.* **73** 25–35
[63] Kang G-D and Cao Y-M 2014 *J. Membr. Sci.* **463** 145–65
[64] Li H-B, Shi W-Y, Zhang Y-F, Liu D-Q and Liu X-F 2014 *Polymers* **6** 1846
[65] Fang Y and Duranceau S 2013 *Membranes* **3** 196